

# Scalable all polymer dielectrics with self-assembled nanoscale multiboundary exhibiting superior high temperature capacitive performance

Received: 12 April 2024

Accepted: 10 October 2024

Published online: 29 October 2024

 Check for updates

Qiyang Zhang<sup>1</sup>✉, Qiaohui Xie<sup>1</sup>, Tao Wang<sup>2</sup>, Shuangwu Huang<sup>1</sup>✉ & Qiming Zhang<sup>3</sup>✉

Polymers are key dielectric materials for energy storage capacitors in advanced electronics and electric power systems due to their high breakdown strengths, low loss, great reliability, lightweight, and low cost. However, their electric and dielectric performance deteriorates at elevated temperatures, making them unable to meet the rising demand for harsh-environment electronics such as electric vehicles, renewable energy, and electrified transportation. Here, we present an all-polymer nanostructured dielectric material that achieves a discharged energy density of 7.1 J/cm<sup>3</sup> with a charge-discharge efficiency of 90% at 150 °C, outperforming the existing dielectric polymers and representing more than a twofold improvement in discharged energy density compared with polyetherimide. The self-assembled nano-scale multi-boundaries effectively impede the charge injection and excitation, leading to more than one order of magnitude lower leakage current density than the pristine polymer matrix PEI at high electric fields and elevated temperature. In addition, the film processing is simple, straightforward, and low cost, thus this all-polymer nanostructured dielectric material strategy is suitable for the mass production of dielectric polymer films for high-temperature capacitive energy storage.

Film capacitors, comprising polymer dielectric films sandwiched between metallic electrodes, are characteristic of ultrahigh power density, fast charge-discharge rates, high-voltage endurance, low energy loss, great reliability and ease of processing, and low cost, establishing them as critically important elements in modern electronic devices and power systems<sup>1–5</sup>. However, polymer dielectrics are limited to relatively low working temperatures, and thus their film capacitors fail to meet the demand for operating stably under harsh-temperature conditions over 140 °C present in applications such as

electric vehicles, aerospace power electronics and underground oil/gas exploration<sup>6–12</sup>. For example, the best commercial capacitor films represented by biaxially oriented polypropylene (BOPP) can operate at temperatures below 105 °C<sup>13</sup>. When the temperature is higher than 85 °C, BOPP film capacitors need to have a 30–50% voltage derating, owing to the extreme deterioration of performance and lifetime<sup>14,15</sup>.

During the past decades, substantial efforts have been made to exploit a variety of engineering polymers with high glass-transition temperature ( $T_g > 150$  °C) for high-temperature film capacitors<sup>16,17</sup>. It

<sup>1</sup>State Key Laboratory of Radio Frequency Heterogeneous Integration, College of Electronics and Information Engineering, Institute of Microelectronics (IME), Shenzhen University, Shenzhen, China. <sup>2</sup>College of Materials Science and Engineering, Shenzhen University, Shenzhen, China. <sup>3</sup>School of Electrical Engineering and Computer Science, Materials Research Institute, The Pennsylvania State University, University Park, PA, USA. ✉e-mail: [zhangqy@szu.edu.cn](mailto:zhangqy@szu.edu.cn); [mark\\_huang@szu.edu.cn](mailto:mark_huang@szu.edu.cn); [qxz1@psu.edu](mailto:qxz1@psu.edu)

was found that on the one hand,  $T_g$  is the key parameter for high-temperature dielectric polymers<sup>7</sup>, as the temperature above  $T_g$ , polymers lose their electromechanical and dimensional stability and exhibit large variations in dielectric performance with temperature. On the other hand, although these high- $T_g$  polymers work reasonably well at low electric fields and high temperatures, the sharp increase of leakage current at high electric fields (>300 MV/m) and high temperature causes large conduction loss and a large reduction of the breakdown field, resulting in poor charge-discharge efficiencies ( $\eta$ ) and low discharge energy density ( $U_e$ )<sup>9</sup>, even at the temperature is well below  $T_g$  of the polymers. Therefore, suppressing the generation and transport of charge carriers at high applied electric and thermal fields in high- $T_g$  dielectric polymers, which cause an exponential increase of leakage current, is essential for high-temperature dielectric capacitors.

To address this challenge, several innovative approaches<sup>1,3,4,6,11,18–24</sup> have been developed that effectively hinder electrical conduction, and achieve high  $\eta$  and  $U_e$  at elevated-temperature and high electric field. Incorporating wide bandgap inorganic nano-fillers such as boron nitride nanosheets (BNNS)<sup>7,25</sup> and  $\text{Al}_2\text{O}_3$ <sup>9,26,27</sup> and high-electron-affinity molecular semiconductors<sup>11,28,29</sup> into polymers to form the polymer composites results in more than one order of magnitude reduction in the conductivity and substantially increased capacitive performance at elevated temperatures. Controlling arrangement or orientation of nanofillers in polymers or surface-coated inorganic layers in the polymer films to fabricate stratified<sup>20</sup> or multilayer polymer films<sup>19,21–23</sup> show effective in impeding the charge injection and transport and results in significant reduction of conduction loss and improvement of  $U_e$  and  $\eta$  at elevated temperatures and high electric field. Facile monomer design and synthesis<sup>6,10,30</sup> and crosslinking of polymers<sup>31,32</sup>, which introduce deep traps, also present effective in improving capacitive performance at elevated temperatures and high electric fields. However, there are substantial challenges in translating these strategies for producing large-scale/low-cost high-performance dielectric polymer films for commercial applications<sup>1</sup>. The introduction of inorganic nanofillers, suffers from low yields and high-cost nanofillers, uniformity, and repeatability of polymer nanocomposite films due to poor compatibility of nanofillers with polymers. The high loading of nanofillers even causes voids and cracks in polymer films and deteriorates film properties and processability. Other strategies, such as multilayer fabrication, monomer synthesis, and crosslinking, require multistep, complex, and low yields manufacturing processes, which make mass production of these polymer dielectric films difficult.

Polymerization-induced microphase separation (PIMS)<sup>33–37</sup> is a useful and widely used strategy to develop unique nanostructured materials through the microphase separation of emergent block copolymers or blends of thermoplastic/thermoset systems during polymerization. In this process, nanostructures are formed with two chemically independent domains, where one domain is composed of a robust crosslinked polymer. In high voltage insulators, barriers formed between two dielectrics of different band structures have been shown effective in blocking charge injection. We hypothesize that dielectric polymer films with the self-assembled nano-scale multiboundary in dielectrics can be effective in impeding the charge excitation and transport even under high temperature and high electric field, which is similar to multilayer containing inorganic layers.

In this work, we demonstrate that the PIMS strategy can be effectively applied to prepare highly scalable and low-cost high-temperature all-polymer nanostructured dielectrics (PNDs). The PNDs with self-assembled nano-scale multiboundary based on the blends of high- $T_g$  engineering polymers and thermosetting resin monomers exhibit superior high-temperature capacitive performance. We chose polyetherimide (PEI)<sup>38</sup> as the high- $T_g$  engineering polymer, which is commercially used in high-temperature film capacitors owing to its high glass transition temperature ( $T_g \approx 217$  °C) and easy processability. A commercial bismaleimide (BMI)<sup>39</sup> monomer (2,2-bis(4-(4-maleimido-

phenoxy)phenyl)propane), which has a band structure with large a band gap ( $E_g$ , e.g., 5.74 eV) and low electron affinities ( $\chi = 0.60$  eV), thus forms high electron injection barrier at contact with PEI (Fig. 1a), was selected as thermosetting resin monomers, see Fig. 1b for BMI molecular structure. In addition, BMI has good compatibility with PEI due to their both having bisphenol A and imide groups in the molecular structure and is widely used in microelectronics and aerospace. Indeed, the experimental results show that the self-assembled nano-scale multiboundary structure effectively impedes the charge injection and excitation, leading to more than 10 times reduction of leakage current at high temperature and high fields, 30% enhancement in the breakdown fields at high temperature (150 °C), compared with neat PEI. Consequently, such an all-polymer nanostructured dielectric material with self-assembled nano-scale multiboundary exhibits discharged energy density of  $7.1 \text{ J cm}^{-3}$  with a charge-discharge efficiency of 90% at 150 °C, outperforming the existing dielectric polymers<sup>6,11,28,32,40–42</sup> and showing a more than two-fold increase in discharged energy density compared to neat PEI. Moreover, compared to the approaches reported in the literature, film processing is much simpler, straightforward, and low-cost, paving the way for mass fabrication of high-performance and high-quality polymer films required for high-temperature film capacitors.

## Results

### Fabrication of PNDs and structural characterization

The fabrication pathway of all-polymer nanostructured dielectrics is presented in Fig. 1c and d, which involves blending BMI monomers with high- $T_g$  PEI to form a homogeneous solution, polymerization-induced microphase separation, and in-situ crosslinking to form well-defined nanostructured dielectric films. The BMI monomer is first blended with a high- $T_g$  PEI to form a homogeneous solution. Then, the blended film precursors comprising high- $T_g$  PEI with BMI monomers are prepared by solution casting of the above homogeneous solution. Upon being subjected to heat treatment at temperatures between 170 and 200 °C, BMI monomers embedded in the blended film precursors would melt and flow between the molecular chains of the high- $T_g$  PEI matrix, due to their lower melting points than the heating temperature; simultaneously, the in-situ free radical polymerization of the BMI monomers is triggered, inducing the chain-extension reaction and cross-linking reaction of maleimide double bonds, and nano-sized phase separation occurs at a critical conversion. After post-curing at a temperature over 200 °C, more maleimide double bonds are converted into bonding points by in-situ crosslinking, forming a dense cross-linking network that endows the resulting well-defined PNDs with robust structural stability and flexibility.

A series of structural characterizations were carried out on the nanostructures formed. Figure 1e presents scanning electron microscope (SEM) images of the cryo-fractured surface of PNDs, revealing that percolated nanodomains with an average particle size of about 60 nanometers are evenly distributed through the dielectric material, forming the self-assembled nano-scale multiboundary. The percolated nanodomains (crosslinked BMI) are produced by a spinodal decomposition process, and the coarsening of the BMI nanodomains is kinetically restricted by the high viscosity of high- $T_g$  engineering polymeric frameworks (e.g., PEI). Presented in Fig. 1f are TEM images showing the percolated BMI nanodomains in PNDs. In PND materials, the interfacial area is directly proportional to the BMI sphere content and inversely proportional to their diameter. The interfacial area coefficient is defined as the ratio of content to diameter. As shown in Figure S1, although the average particle size of BMI domains increases with increasing BMI content, the maximum interfacial area coefficient is achieved at a BMI content of 25 wt.%.

We performed a Fourier transform infrared (FTIR) study of the in-situ free radical polymerization of the BMI monomers in blended film precursors after heat treatment and the results are presented in Fig. 1g.

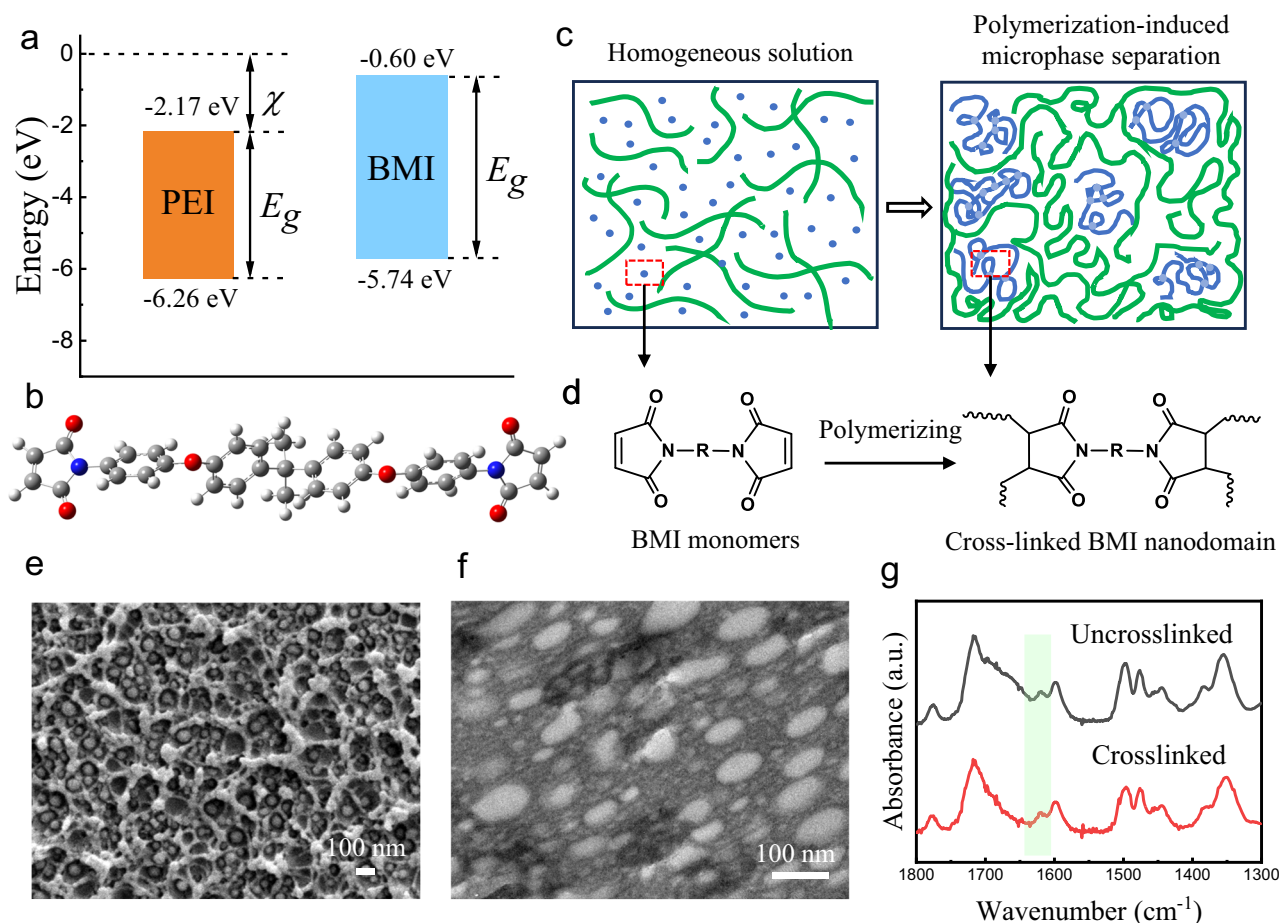


**Fig. 1 | Material preparation and microstructures.** **a** Energy-band diagram of PEI and BMI.  $\chi$  represents the electron affinity, and  $E_g$  denotes the band gap. **b** Molecular structure of the BMI monomer. **c** Schematic of the preparation of PND films by a polymerization-induced microphase separation process. **d** In-situ free

radical polymerization of the BMI monomers. **e** Scanning electron microscopy (SEM) image and **(f)** Transmission Electron Microscopy (TEM) image of a PEI/BMI PND film. **(g)** Fourier transform infrared spectra of pristine and crosslinked BMIs in PEI/BMI PND films.

The peak around  $1620\text{ cm}^{-1}$  is from the stretching vibration of C=C in BMI, which is greatly reduced after in-situ cross-linking, indicating that most of the C=C bonds had been polymerized<sup>43</sup>. Furthermore, differential scanning calorimetry (DSC) and X-ray diffraction (XRD) were employed to characterize the aggregation structure. The PNDs exhibited higher  $T_g$  than the pristine PEI molecular network (Figure S2a), owing to the good compatibility between crosslinked BMI nanodomain and PEI matrix enabled by similar molecular structure. The enhanced  $T_g$  originates from a strong intermolecular interaction between the BMI nanodomains and the PEI molecular network. XRD data reveal that the PNDs exhibit a broad amorphous scattering peak at a higher  $2\theta$  angle (Figure S2b), which corresponds to the smaller interchain spacing. A substantially increased elastic modulus of PNDs, compared with pristine PEI, is also observed (Figure S2c), consistent with the dense cross-linking network in BMI nanodomains and good compatibility between BMI nanodomains and PEI matrix. The enhanced elastic modulus of the polymers will favor the increase of their dielectric breakdown strength, as the elastic modulus of polymers plays a vital role in determining the breakdown strength according to the electromechanical breakdown mechanism<sup>44</sup>. The percolated BMI nanodomains with the dense cross-linking network in the PEI matrix lead to a much lower coefficient of thermal expansion, as shown in Figure S2d.

### Dielectric properties and energy storage performance

We characterized the dielectric properties of the PNDs and the neat PEI as functions of temperature and frequency. As presented in Figure S3,

the PNDs show stable dielectric constant  $K$  and dissipation factor  $DF$  in temperatures to  $200\text{ }^\circ\text{C}$  and frequency range  $10\text{--}10^6\text{ Hz}$  (Figure S3b). In the frequency range of  $0.1\text{--}1\text{ Hz}$ , both the  $K$  and the  $DF$  of PND and pure PEI show slight increase with reduced frequency. This indicates the presence of interfacial polarization in both PNDs and PEI at low frequencies. The capacitive energy storage performances of PNDs at elevated temperatures were characterized by electric displacement–electric field (D–E) loops (Figs. S4 & S5). The slimmer D–E loops of the PNDs are indicative of lower energy loss than that of pristine PEI. The assessment is particularly focused on the  $U_e$  achieved at a high  $\eta$  level (i.e.,  $>90\%$ )<sup>11</sup>. As shown in Fig. 2, the PND with composition of PEI/BMI 75/25 exhibit substantially enhanced  $U_e$  and  $\eta$  at elevated temperatures, in comparison to those of pristine PEI. The high  $\eta$  of the PND at elevated temperature corresponds to the slim D–E loop in contrast to the lossy one in pristine PEI (Fig. 2b–f). At  $150\text{ }^\circ\text{C}$ , the PND with composition of PEI/BMI 75/25 delivers a discharged energy density  $U_e$  exceeding  $7.1\text{ J cm}^{-3}$  with  $\eta$  of larger than  $90\%$ , whereas that of the pristine PEI is  $3.1\text{ J cm}^{-3}$ . More remarkably, at  $200\text{ }^\circ\text{C}$ , the PND with composition of PEI/BMI 75/25 generates an  $U_e$  of  $4.4\text{ J cm}^{-3}$  with  $\eta$  of larger than  $90\%$ , which is over twice that of pristine PEI (i.e.,  $1.7\text{ J cm}^{-3}$ ). Notably, the PND in this work stands out from both the commercially available capacitor films and the latest reported all-organic dielectric polymers at  $150\text{ }^\circ\text{C}$  (Fig. 2c)<sup>6,11,28,32,40–42</sup> due to its high  $U_e$  and low-cost and straightforward film processing. In particular, such high  $U_e$  of the PND at  $\eta > 90\%$  achieved at  $200\text{ }^\circ\text{C}$  is also higher than that of BOPP ( $4.0\text{ J cm}^{-3}$ ) at the room-temperature<sup>11</sup>. Figures S8 and S9 present the discharge energy density and charge-discharge efficiency of PNDs with

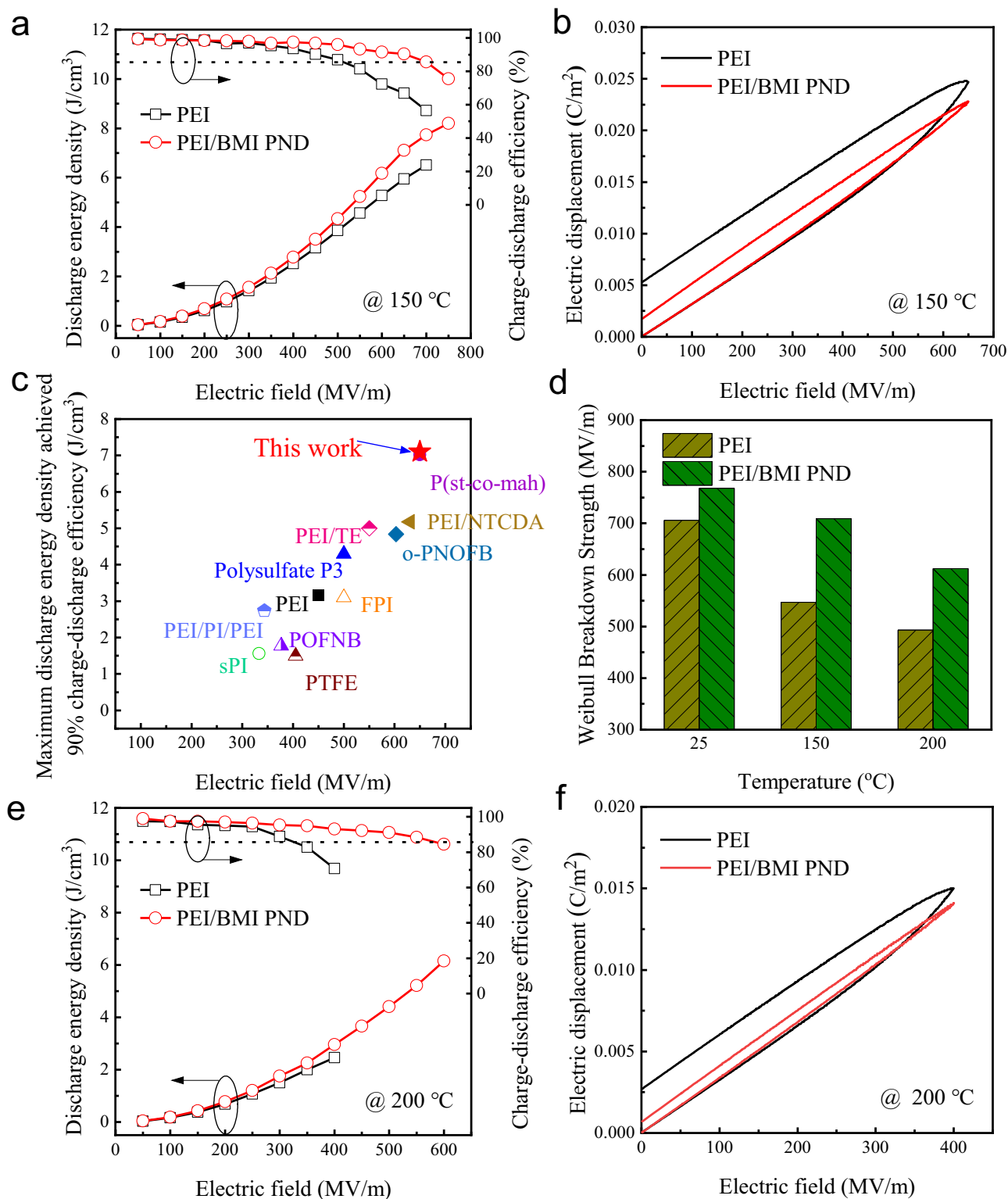


**Fig. 2 | High-temperature energy storage performance of the PNDs.** **a** Field-dependent energy density and discharge efficiency of pristine PEI and the PND with composition of PEI/BMI 75/25 at  $150^\circ\text{C}$ . **b** Comparison of electric displacement-electric field (D-E) loops at  $650\text{ MV/m}$  and  $150^\circ\text{C}$ . **c** Comparison of the maximum discharged energy density at  $150^\circ\text{C}$  and above 90% efficiency of the PND with composition of PEI/BMI 75/25 and other reported high-temperature dielectric

polymers. **d** Weibull breakdown strength ( $E_b$ ) of pristine PEI and the PND with composition of PEI/BMI 75/25 measured at different temperatures. **e** Field-dependent energy density and discharge efficiency of pristine PEI and the PND with composition of PEI/BMI 75/25 at  $200^\circ\text{C}$ . **f** Comparison of electric displacement-electric field (D-E) loops at  $400\text{ MV/m}$  and  $200^\circ\text{C}$ .



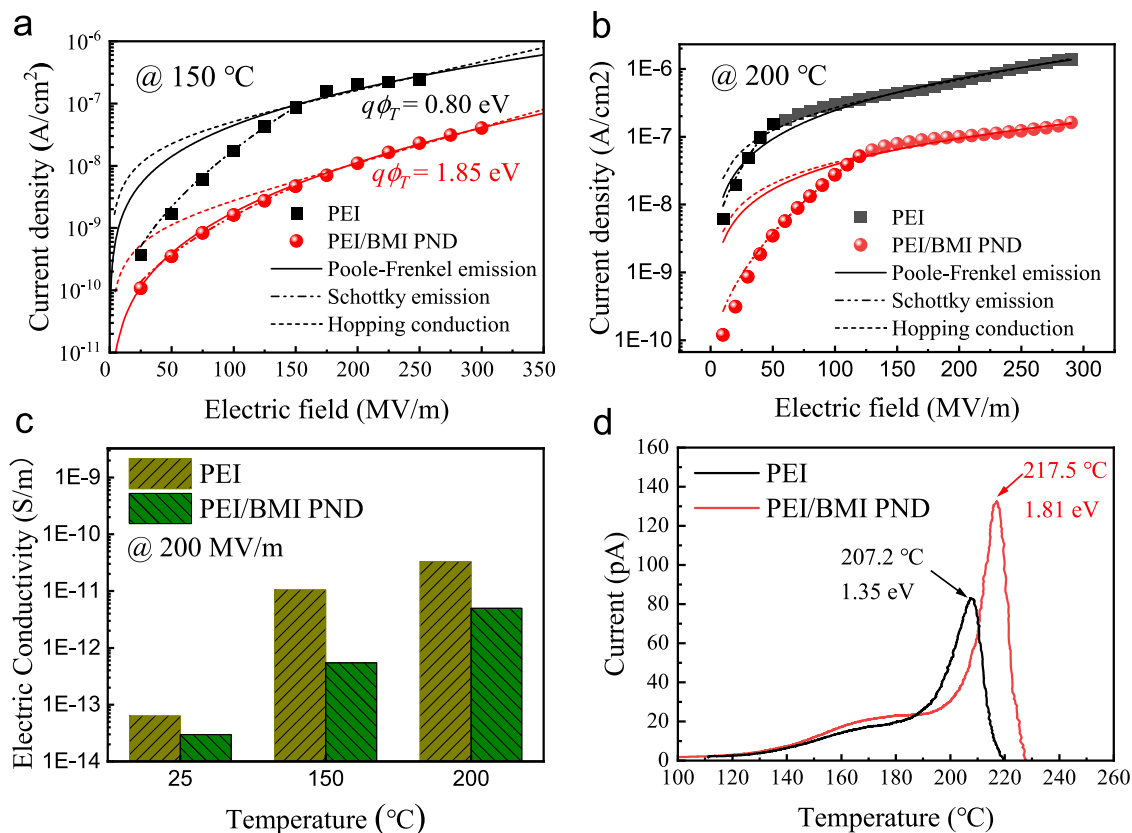


**Fig. 3 | Electrical properties of the PND with composition of PEI/BMI 75/25 and compared with pristine PEI.** Electric field-dependent conduction current density at (a) 150 °C and (b) 200 °C. c Electrical conductivity under 200 MV/m at different temperatures. d TSDC spectra.

different BMI contents. The highest discharged energy density and charge-discharge efficiency are achieved at a BMI content of 25 wt%, which also corresponds to the maximum interfacial area coefficient (Figures S1d). These results indicate the significant role of self-assembled nano-scale multiboundaries in enhancing high-temperature dielectric energy storage performance.

The dielectric breakdown process of the PNDs was measured at elevated temperatures, with  $E_b$  determined by a two-parameter Weibull statistical analysis. Figures 2d and S6 compare the  $E_b$  and characteristic breakdown parameters ( $\beta$  value) at different temperatures of the PND and pristine PEI. Notably, the PND exhibits improved  $E_b$  compared with the pristine PEI, especially at elevated temperatures (Fig. 2d). For instance, at 150 °C, the PND has an  $E_b$  of 709 MV/m, while the pristine PEI is only 550 MV/m. The  $E_b$  of PND at 150 °C is also higher than those of most of currently reported high-temperature polymers, such as 377 MV/m for PEI<sup>12</sup>, 400 MV/m for PEEU<sup>9</sup> and 641 MV/m for CS-ODA<sup>29</sup> (Fig. S7). Additionally, a pronounced increase of the  $\beta$  value is found in the PND, e.g., 27.6 of PND *vs.* 16.9 of pristine PEI at 150 °C, and 45.5 of PND *vs.* 19.7 of pristine PEI at 200 °C, denoting an increased dielectric reliability of the PND films.

The PND films also outperform the pristine PEI matrices in cyclic charge-discharge tests, indicative of greater long-term stability and reliability at high temperatures and high electric fields. During over 50 000 charge-discharge cycles at 150 °C and 400 MV/m (much higher than operating condition, i.e., 200 MV/m, of capacitors in common power systems such as electric vehicles), the  $U_c$  of the PND only fluctuates within a slight variation of 0.45% and  $\eta$  maintains at an ultrahigh level of > 95%. By contrast, the pristine PEI can operate only up to 51 cycles at 150 °C and 400 MV/m, respectively (Fig. S10). The enhanced durability is attributed to the significantly higher electric breakdown strength of PND (Weibull  $E_b$  709 MV/m) compared to PEI (547 MV/m). These results suggest that the PND is of great promise for reducing

waste heat and prolonging the service life of dielectrics in practical applications.

We evaluated the ability of PND to form uniform, high-quality films by casting large PND films with dimensions of 20 cm × 30 cm. We measured the breakdown strength and discharged energy density at different regions of the film at 150 °C. The results showed high consistency across the different regions (Fig. S11), indicating that the film was uniformly manufactured without uniformity issues. These findings suggest that PND is suitable for the mass production of large-area, high-quality films.

### Electrical conduction and charge trapping

The superior performance of PNDs over the high- $T_g$  PEI matrix stems from its substantially reduced high-field leakage current at elevated temperatures. Figure 3a and b shows the dependence of the leakage current density of the PNDs on the applied field at 150 °C and 200 °C, and compared with pristine PEI. Obviously, the current density of PNDs is much lower than that of pristine PEI at all the measured electric fields, for example, the leakage current density decreases from  $2.1 \times 10^{-7}$  A/cm<sup>2</sup> of pristine PEI to  $1.09 \times 10^{-8}$  A/cm<sup>2</sup> of PNDs at 200 MV/m and 150 °C. PNDs exhibit more than one order of magnitude lower electrical conductivity than that of pristine PEI at 200 MV/m and elevated temperatures (Fig. 3c).

The high-field leakage current results confirm that the PND films with self-assembled nano-scale multiboundary are capable of impeding electrical conduction, especially at high electric fields. We used the thermally stimulated depolarization currents (TSDC) to characterize the possible deep traps in PNDs and comparison with the pristine PEI. As presented in Fig. 3d, the depolarization current peak corresponding to the de-trapping of charge carriers in all-polymer nanostructured dielectrics is located at a higher temperature than that of pristine PEI. The trap energy level is calculated from TSDC curves according to the

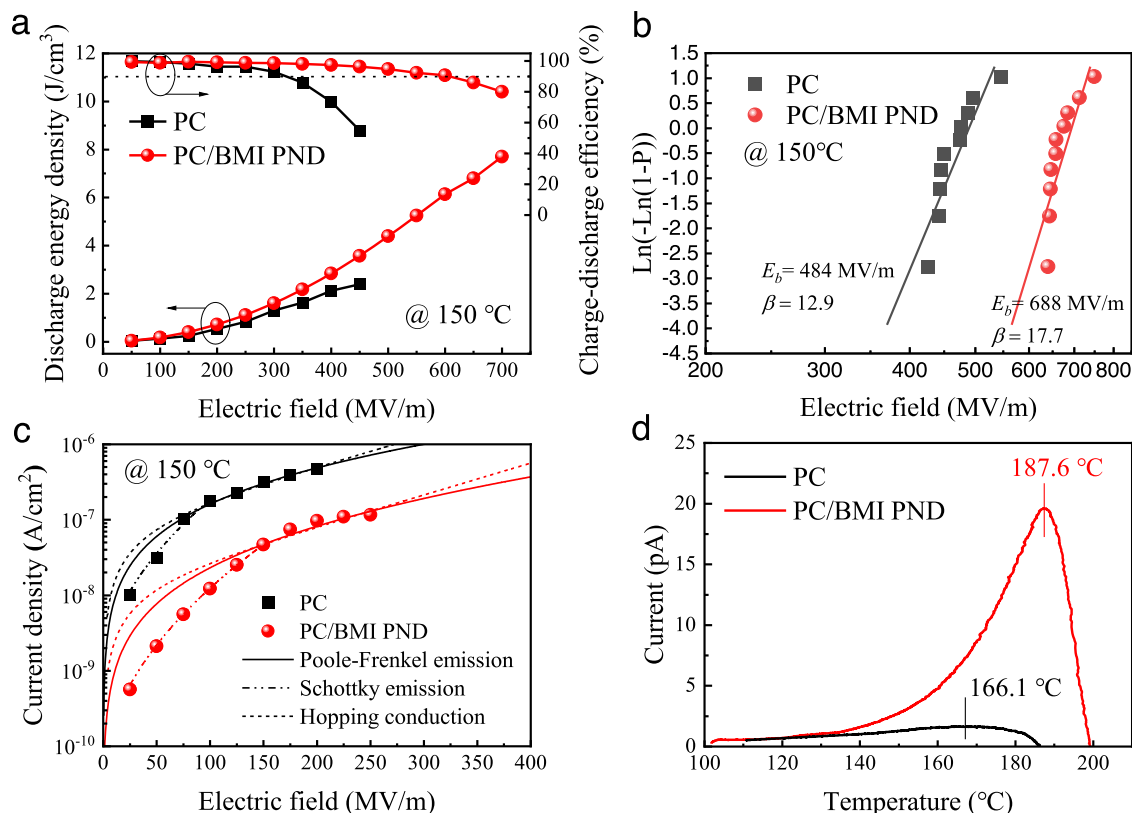


**Fig. 4 | Capacitive energy storage and electric performance of PC/BMI PNDs.** **a** Field-dependent energy density and discharge efficiency. **b** Weibull breakdown strength ( $E_b$ ) of pristine PC and the PC/BMI PND with composition of PC/BMI 80/20

at 150 °C. **c** Electric field-dependent conduction current density, and **(d)** TSDC spectra of pristine PC and the PC/BMI PND with composition of PC/BMI 80/20 measured at different temperatures.

initial rise method<sup>45</sup> (Fig. S12). A larger trap depth of 1.81 eV was determined for the PND compared with neat PEI (1.35 eV), suggesting the critical role of self-assembled nano-scale multiboundary in introducing deep traps in the polymer, which inhibits the mobile charges when excited at high electric fields and elevated temperatures.

We used the trap levels determined from TSDC and the bulk phase limited Pooler-Frenkel emission<sup>46</sup> to fit the leakage currents of PNDs as well as the neat PEI. As shown in Fig. 3a and b, the fitting curves match the measured leakage currents of the PND well, especially at electric fields higher than 100 MV/m (the solid curves). In contrast, such fitting using a trap depth of 1.35 eV does not match the leakage currents of neat PEI, suggesting other conduction processes such as carrier hopping may also be present, which generated a high leakage current. Figure 3c presents the electrical conductivity  $\sigma$  under 200 MV/m measured at various temperatures. PND exhibits much lower  $\sigma$  at high temperatures, compared with the neat PEI.

The TSDC in conjunction with the leakage current density results corroborate that the self-assembled nano-scale multiboundary in all-polymer nanostructured dielectrics have major impacts on the charge injection, excitation, and capture in dielectric polymers, which are effective in immobilizing the free charges. The low leakage current density and low electrical conductivity of PNDs resulted in the high-temperature capacitive performance in terms of  $U_e$ ,  $\eta$ , and  $E_b$  as shown in the experimental results above-mentioned.

In addition to lowering the leakage current, the PND also exhibited a higher elastic modulus than the neat PEI, as presented in Figure S2c, which may also play a role in the higher  $E_b$  of PND than that of PEI, considering the electromechanical (EM) breakdown in polymers. The EM breakdown is caused by the electrostatic force from the charges at the electrodes and hence the breakdown strength is proportional to  $\sqrt{Y/K}$ , where  $Y$  is the elastic modulus and  $K$  is the

dielectric constant<sup>47</sup>. From Figs. 2d and S2c, the increased  $Y$  of PND is too small to account for the observed increase of  $E_b$  of PND, especially at high temperatures. In addition,  $E_b$  deduced from the EM breakdown is much higher than that in Fig. 2f.

#### Energy storage and electric performance of PC-based PNDs

To demonstrate the versatility of the PIMS approach, in addition to PEI, another high- $T_g$  dielectric polymer, polycarbonate (PC,  $T_g \approx 180$  °C), was also employed as a matrix to prepare PNDs with self-assembled nano-scale multiboundary. As shown in Fig. 4, in analogy with the PEI-based PNDs, the PC-based PNDs also exhibit significant improvement in capacitive energy storage and electric performance. Specifically, PC-based PNDs discharged an  $U_e$  exceeding 6.1 Jcm<sup>-3</sup> with  $\eta$  of larger than 90% at 150 °C, whereas that of the pristine PC was 1.4 Jcm<sup>-3</sup>. The  $E_b$  was increased from 484 MV/m of pristine PC to 688 MV/m of PC-based PNDs at 150 °C. The enhancement of PC-based PNDs also stems from its substantially reduced high-field leakage current at elevated temperatures. The PC-based PNDs exhibit more than one order of magnitude lower leakage current density than that of pristine PC at 150 °C, for example, the leakage current density decreases from  $4.78 \times 10^{-7}$  A/cm<sup>2</sup> of pristine PC to  $9.66 \times 10^{-8}$  A/cm<sup>2</sup> of PC-based PNDs at 200 MV/m. The PC-based PNDs also have much deeper trap depth and trap density compared to pristine PC, as shown in the TSDC curves with increased intensity of depolarization current peak and peak temperature.

#### Discussion

In summary, we demonstrated all-polymer nanostructured dielectric materials with self-assembled nano-scale multiboundary prepared by polymerization-induced nano-sized phase separation in the blends of high- $T_g$  engineering polymers and a thermosetting BMI resin. The all-polymer nanostructured dielectric materials showed significantly

enhanced high-temperature capacitive performance that outperforms most current dielectric polymers. The percolated self-assembled nanoscale multiboundary in PNDs impedes the charge injection and excitation of the mobile charges, resulting in the substantially reduced high-field leakage current at elevated temperatures and marked improvements in the high-temperature capacitive energy storage properties. Since the raw materials (e.g., BMI monomers and high  $T_g$  polymers) are readily accessible and very low cost, and the film processing is simple and straightforward, this all-polymer nanostructured dielectric materials strategy has the promise to address the challenge in scalable fabrication of high-performance and high-quality polymer films required for high-temperature capacitive energy storage.

## Methods

### Materials

PEI (Utem 1000) and PC (HT200) were provided by PolyK Technologies, United States. Bis(tert-butylidioxisopropyl)benzene (BIPB, 98.0%), Dimethylformamide (DMF, 99.5%), N-Methyl pyrrolidone (NMP, 99.5%), and 2,2-Bis[4-(4-maleimidophenoxy)phenyl]propane (BMI, 98.0%) were purchased from Aladdin Chemistry Co., Ltd., China. All chemicals were used directly without further treatment.

### Preparation of PND films

To prepare the PEI/BMI-based PND films, a 200 mg mixture consisting of PEI pellets and BMI monomers in specified ratios (e.g., 100/0, 95/5, 75/25, 60/40, etc.), along with 1 wt.% BIPB relative to the BMI content, was dissolved in 10 ml of NMP. The solution was stirred at 70 °C for 12 hours until it became clear and homogeneous. The solution was drop-casted on a clean glass slide and kept in a drying oven at 80 °C for 12 hours to remove the solvent. Afterward, the films were further heated at 180 °C for 2 hours, 200 °C for 2 hours, and 230 °C for 4 hours under vacuum to trigger the polymerization of BMI monomers to obtain nano-size separation of crosslinked BMIs with PEI matrix, as well as to further remove any residual solvent. The cast film was peeled off from the glass substrate in deionized water and then dried at 200 °C in a vacuum oven for another 12 h to obtain the free-standing films. To prepare the PC/BMI-based PND films, a 200 mg mixture of PC powers and BMI monomers in specified ratios (e.g., 100/0 and 80/20), along with 1 wt.% BIPB relative to the BMI content, was dissolved in 10 ml of DMF. The solution was stirred at 70 °C for 12 hours until clear and homogeneous. It was then drop-cast onto a clean glass slide and placed in a drying oven at 70 °C for 12 hours to evaporate the solvent. The subsequent steps followed the same procedure as for the preparation of PEI/BMI-based PND films.

### Structural characterizations

Cryo-fractured cross-sectional micromorphology was examined with focused ion beam-scanning electron microscopy (FIB-SEM) (FEI Scios, Thermo Fisher). To study the phase morphologies of BMI domains, thin film samples were prepared using an ultramicrotome and analyzed with a TECNAI G2-F20 transmission electron microscope (TEM). Fourier-transform infrared (FTIR) spectroscopy was conducted on a Nicolet iS10 (Thermo Scientific) FTIR spectrometer. Differential scanning calorimetry (DSC) measurements were performed under a nitrogen atmosphere using a PerkinElmer DSC 4000, heating and cooling rates of 10 °C/min. X-ray diffraction (XRD) analysis was carried out on a Rigaku MiniFlex600 diffractometer (Cu  $K\alpha$  source, wavelength = 1.54 Å). The storage modulus of the films was determined using a dynamic mechanical analyzer (DMA850, TA Instruments). The coefficient of thermal expansion was measured with a TMA Q400 thermal mechanical analyzer (TA Instruments).

### Dielectric and electrical measurements

The thickness of films used for electrical characterizations was in the range of 10–15  $\mu\text{m}$ . Gold electrodes (a diameter of 6 mm and

thicknesses of 60 nm) were sputtered on both sides of the polymer films for electrical measurements. Broadband dielectric spectroscopy was conducted using a Novocontrol Concept 80 Dielectric Spectrometer. Dielectric temperature spectra were measured from 25 °C to 200 °C for PEI/BMI-based PNDs and from 25 °C to 160 °C for PC/BMI-based PNDs using a Keysight E4980AL LCR meter in conjunction with a Sun Systems environment chamber. The breakdown strengths were measured using Trek 610E, United States. The temperature was controlled by a digital hot plate. The displacement-electric field (D-E) loops were measured using a modified Sawyer-Tower circuit under a unipolar triangle voltage with a frequency of 100 Hz. The cyclic charge–discharge tests were performed by a PK-CPRI502 test system from PolyK Technologies, United States.

Conduction currents were measured using a Keithley 6517B pA meter and a Trek 610E amplifier. The TSDC was collected by a PK-SPIV17 measurement system (PolyK Technologies, United States). The PEI/BMI-based PND samples were polarized at 230 °C under a 50 MV  $\text{m}^{-1}$  field. Afterwards, the temperature was cooled to 100 °C at a rate of 20 °C  $\text{min}^{-1}$  under the applied field and then the electric field was removed. TSDC current was measured using a Keithley 6517B electrometer at a heating rate of 3 °C  $\text{min}^{-1}$ . The PC/BMI-based PND samples were polarized at 200 °C under a 20 MV  $\text{m}^{-1}$  field. After polarization, the sample was cooled to 100 °C at a rate of 20 °C  $\text{min}^{-1}$  under electric field and then the field was removed. TSDC current was measured using a Keithley 6517B electrometer at a heating rate of 3 °C  $\text{min}^{-1}$ .

### DFT calculations

Density functional theory (DFT) calculations were performed using the Gaussian 09 (Rev D.01). DFT is based on the first-principles calculation and the wave functions of calculated molecules are determined according to the solution of basic Schrodinger's equation. In this work, all geometries were fully optimized without symmetry constraints, utilizing the B3LYP functional and 6-31G(d,p) basis set. The convergence criteria for geometry optimization specified a maximum force of less than 0.00045 Hartree/Bohr and a maximum displacement of less than 0.0018 Bohr. Frequency calculations were performed to verify that the optimized structures correspond to true minima, with no imaginary frequencies. The HOMO and LUMO energy levels were calculated based on the optimized ground state geometries. All calculations were performed under vacuum conditions, excluding any solvent effects in the model.

### Data availability

The data that support the findings of this study are included within the paper and its Supplementary Information file/Source Data file. Any other relevant data are available from the corresponding authors upon request. Source data are provided with this paper.

### References

1. Shen, Y., Zhang, X., Li, M., Lin, Y. & Nan, C. W. Polymer nanocomposite dielectrics for electrical energy storage. *Nat. Nanotechnol.* **19**, 588–603 (2024).
2. Chen, J. et al. Engineering the dielectric constants of polymers: from molecular to mesoscopic scales. *Adv. Mater.* 2308670 (2023).
3. Zhang, T. et al. Recent progress in polymer dielectric energy storage: From film fabrication and modification to capacitor performance and application. *Prog. Mater. Sci.* **140**, 101207 (2023).
4. Pei, J. Y., Yin, L. J., Zhong, S. L. & Dang, Z. M. Suppressing the loss of polymer-based dielectrics for high power energy storage. *Adv. Mater.* **35**, 2203623 (2022).
5. Luo, H. et al. Progress on polymer dielectrics for electrostatic capacitors application. *Adv. Sci.* **9**, 2202438 (2022).
6. Zhu, Y. et al. Ladderphane copolymers for high-temperature capacitive energy storage. *Nature* **615**, 62–66 (2023).

7. Li, Q. et al. Flexible high-temperature dielectric materials from polymer nanocomposites. *Nature* **523**, 576–579 (2015).
8. Yang, M. et al. Roll-to-roll fabricated polymer composites filled with sub-nanosheets exhibit high energy density and cyclic stability at 200 °C. *Nat. Energy* **9**, 143–153 (2024).
9. Zhang, T. et al. A highly scalable dielectric metamaterial with superior capacitor performance over a broad temperature. *Sci. Adv.* **6**, eaax6622 (2020).
10. Wang, R. et al. Designing tailored combinations of structural units in polymer dielectrics for high-temperature capacitive energy storage. *Nat. Commun.* **14**, 2406 (2023).
11. Yuan, C. et al. Polymer/molecular semiconductor all-organic composites for high-temperature dielectric energy storage. *Nat. Commun.* **11**, 3919 (2020).
12. Zhang, Q. et al. High-temperature polymers with record-high breakdown strength enabled by rationally designed chain-packing behavior in blends breakdown strength enabled by rationally designed. *Matter* **4**, 1–12 (2021).
13. Rabuffi, M. & Picci, G. Status quo and future prospects for metalized polypropylene energy storage capacitors. *IEEE Trans. Plasma Sci.* **30**, 1939–1942 (2002).
14. Johnson, R. W., Evans, J. L., Jacobsen, P., Thompson, J. R. & Christopher, M. The changing automotive environment: High-temperature electronics. *IEEE Trans. Electron. Packag. Manuf.* **27**, 164–176 (2004).
15. Ho, J. & Jow, T. R. High field conduction in biaxially oriented polypropylene at elevated temperature. *IEEE Trans. Dielectr. Electr. Insul.* **19**, 990–995 (2012).
16. Ho, J. S. & Greenbaum, S. G. Polymer capacitor dielectrics for high temperature applications. *ACS Appl. Mater. Interfaces* **10**, 29189–29218 (2018).
17. Li, Q. et al. High-temperature dielectric materials for electrical energy storage. *Annu. Rev. Mater. Res.* **48**, 219–243 (2018).
18. Wu, F. et al. Inorganic–organic hybrid dielectrics for energy conversion: mechanism, strategy, and applications. *Adv. Funct. Mater.* **33**, 2212861 (2023).
19. Zhou, Y. et al. A scalable, high-throughput, and environmentally benign approach to polymer dielectrics exhibiting significantly improved capacitive performance at high temperatures. *Adv. Mater.* **30**, 1805672 (2018).
20. Wu, C. et al. Scalable self-assembly interfacial engineering for high-temperature dielectric energy storage. *iScience* **25**, 104601 (2022).
21. Dong, J. et al. A facile in situ surface-functionalization approach to scalable laminated high-temperature polymer dielectrics with ultrahigh capacitive performance. *Adv. Funct. Mater.* **31**, 2102644 (2021).
22. Zhuo, J., Lin, M., Zhang, Q. & Huang, S. Design, fabrication, and high-temperature dielectric energy storage performance of thermoplastic polyimide/aluminum oxide sandwich-structured flexible dielectric films. *Acta Phys. Sin.* **73**, 177701 (2024).
23. Lin, M., Zhuo, J., Huang, S., Zhang, Q. & Zhang, Q. M. Sandwich-structured polymer dielectrics exhibiting significantly improved capacitive performance at high temperatures by roll-to-roll physical vapor deposition. *Chem. Eng. J.* **498**, 155586 (2024).
24. Zhang, Q. et al. Low-entropy amorphous dielectric polymers for high-temperature capacitive energy storage. *Energy Environ. Sci.* <https://doi.org/10.1039/D4EE02455A> (2024).
25. Ai, D. et al. Tuning nanofillers in in situ prepared polyimide nanocomposites for high-temperature capacitive energy storage. *Adv. Energy Mater.* **10**, 1903881 (2020).
26. Li, H. et al. Scalable polymer nanocomposites with record high-temperature capacitive performance enabled by rationally designed nanostructured inorganic fillers. *Adv. Mater.* **31**, 1900875 (2019).
27. Yang, M. et al. Quantum size effect to induce colossal high-temperature energy storage density and efficiency in polymer/inorganic cluster composites. *Adv. Mater.* **35**, 1–9 (2023).
28. Zhou, Y., Zhu, Y., Xu, W. & Wang, Q. Molecular trap engineering enables superior high-temperature capacitive energy storage performance in all-organic composite at 200. C. *Adv. Energy Mater.* **13**, 2203961 (2023).
29. Ren, W. et al. Scalable ultrathin all-organic polymer dielectric films for high-temperature capacitive energy storage. *Adv. Mater.* **34**, 2207421 (2022).
30. Wu, C. et al. Flexible cyclic-ole fi n with enhanced dipolar relaxation for harsh condition electri fi cation. *Proc. Natl Acad. Sci.* **118**, e2115367118 (2021).
31. Li, H. et al. Crosslinked fluoropolymers exhibiting superior high-temperature energy density and charge-discharge efficiency. *Energy Environ. Sci.* **13**, 1279 (2020).
32. Pan, Z. et al. Tailoring Poly(Styrene-co-maleic anhydride) networks for all-polymer dielectrics exhibiting ultrahigh energy density and charge–discharge efficiency at elevated temperatures. *Adv. Mater.* **35**, 2207580 (2023).
33. Seo, M. & Hillmyer, M. A. Reticulated nanoporous polymers by controlled polymerization-induced microphase separation. *Science* **336**, 1422–1425 (2012).
34. Lee, K., Corrigan, N. & Boyer, C. Polymerization induced microphase separation for the fabrication of nanostructured materials. *Angew. Chem. - Int. Ed.* **62**, e202307329 (2023).
35. Inoue, T. Reaction-induced phase decomposition in polymer blends. *Prog. Polym. Sci.* **20**, 119–153 (1995).
36. Oh, T. et al. Polymerization-induced microphase separation of a polymerization mixture into nanostructured block polymer materials. *Prog. Polym. Sci.* **145**, 101738 (2023).
37. Jeong, C. K. et al. Electrical biomolecule detection using nano-patterned silicon via block copolymer lithography. *Small* **10**, 337–343 (2014).
38. Pfeiffenberger, N. et al. High temperature dielectric polyetherimide film development. *IEEE Trans. Dielectr. Electr. Insul.* **25**, 120–126 (2018).
39. Iredale, R. J., Ward, C. & Hamerton, I. Modern advances in bismaleimide resin technology: A 21st century perspective on the chemistry of addition polyimides. *Prog. Polym. Sci.* **69**, 1–21 (2017).
40. Yang, M., Zhou, L., Li, X., Ren, W. & Shen, Y. Polyimides physically crosslinked by aromatic molecules exhibit ultrahigh energy density at 200 °C. *Adv. Mater.* **35**, 2302392 (2023).
41. Zhang, B. et al. Superior high-temperature energy density in molecular semiconductor / polymer all-organic composites. *Adv. Funct. Mater.* **33**, 2210050 (2022).
42. Li, H. et al. High-performing polysulfate dielectrics for electrostatic energy storage under harsh conditions. *Joule* **7**, 95–111 (2023).
43. Ladani, N. K., Mungra, D. C., Patel, M. P. & Patel, R. G. Microwave assisted synthesis of novel Hantzsch 1,4-dihydropyridines, acridine-1,8-diones and polyhydroquinolines bearing the tetrazolo[1,5-a]quinoline moiety and their antimicrobial activity asses. *Thin. Chem. Lett.* **22**, 1407–1410 (2011).
44. Shen, Z. H. et al. Phase-field modeling and machine learning of electric-thermal-mechanical breakdown of polymer-based dielectrics. *Nat. Commun.* **10**, 1843 (2019).
45. Bräunlich, P. Comment on the initial-rise method for determining trap depths. *J. Appl. Phys.* **38**, 2516–2519 (1967).
46. Chiu, F.-C. A review on conduction mechanisms in dielectric films. *Adv. Mater. Sci. Eng.* **9**, 143–153 (2014).
47. Zhou, X. et al. Electrical breakdown and ultrahigh electrical energy density in poly(vinylidene fluoride-hexafluoropropylene) copolymer. *Appl. Phys. Lett.* **94**, 162901 (2009).



## Acknowledgements

Q.Y.Z. was supported by the National Natural Science Foundation of China (grant nos. 52203096) and the Shenzhen Science and Technology Innovation Program (RCBS20221008093110036, ZDSYS20220527171402005). The authors thank the assistance on SEM observation received from the Electron Microscope Center of Shenzhen University.

## Author contributions

QYZ directed the research and designed the experiment. QHX performed experiments. TW performed the DFT calculation. QYZ, SWH, and QMZ participated in the discussion. QYZ and QMZ wrote the paper.

## Competing interests

The authors declare no competing interests.

## Additional information

**Supplementary information** The online version contains supplementary material available at <https://doi.org/10.1038/s41467-024-53674-8>.

**Correspondence** and requests for materials should be addressed to Qiyang Zhang, Shuangwu Huang or Qiming Zhang.

**Peer review information** *Nature Communications* thanks Xingyi Huang, and the other, anonymous, reviewer(s) for their contribution to the peer review of this work. A peer review file is available.

**Reprints and permissions information** is available at <http://www.nature.com/reprints>

**Publisher's note** Springer Nature remains neutral with regard to jurisdictional claims in published maps and institutional affiliations.

**Open Access** This article is licensed under a Creative Commons Attribution-NonCommercial-NoDerivatives 4.0 International License, which permits any non-commercial use, sharing, distribution and reproduction in any medium or format, as long as you give appropriate credit to the original author(s) and the source, provide a link to the Creative Commons licence, and indicate if you modified the licensed material. You do not have permission under this licence to share adapted material derived from this article or parts of it. The images or other third party material in this article are included in the article's Creative Commons licence, unless indicated otherwise in a credit line to the material. If material is not included in the article's Creative Commons licence and your intended use is not permitted by statutory regulation or exceeds the permitted use, you will need to obtain permission directly from the copyright holder. To view a copy of this licence, visit <http://creativecommons.org/licenses/by-nc-nd/4.0/>.

© The Author(s) 2024